We are IntechOpen,
the world's leading publisher of
Open Access books
Built by scientists, for scientists

4,800
Open access books available

122,000
International authors and editors

135M
Downloads

154
Countries delivered to

Our authors are among the

TOP 1%
most cited scientists

12.2%
Contributors from top 500 universities

WEB OF SCIENCE™

Selection of our books indexed in the Book Citation Index
in Web of Science™ Core Collection (BKCI)

Interested in publishing with us?
Contact book.department@intechopen.com

Chapter

Phase Separation in Ce-Based Metallic Glasses

Dharmendra Singh, Kiran Mor, Devinder Singh and Radhey Shyam Tiwari

Abstract

In this chapter, the results of our recent studies on the role of Ga substitution in place of Al in $Ce_{75}Al_{25-x}Ga_x$ (x = 0, 0.01, 0.1, 0.5, 1, 2, 4, and 6) metallic glasses (MGs) have been discussed with the aim to understand the genesis of phase separation. X-ray diffraction (XRD) study reveals two broad diffuse peaks corresponding to the coexistence of two amorphous phases. In order to see any change in the behavior of $4f$ electron of Ce, X-ray absorption spectroscopy (XAS) has been carried out for $Ce_{75}Al_{25-x}Ga_x$ MGs. From the XAS results, it is evident that for x = 0, the spectrum exhibits only a $4f^1$ component, which basically shows a pure localized configuration of electron. After the addition of Ga, $4f$ electrons of Ce atoms denoted by $4f^0$ are getting delocalized. Thus, the phase separation in $Ce_{75}Al_{25-x}Ga_x$ is taking place, owing to the formation of two types of amorphous phases having localized and delocalized $4f$ electrons of Ce atoms, respectively. It has been discussed how change in the electronic structure of Ce atoms may lead to phase separation in $Ce_{75}Al_{25-x}Ga_x$ alloys. Extensive TEM investigations have been done to study the phase separation in these alloys. The microstructural features have been compared with those obtained by phase field modeling.

Keywords: metallic glass, phase separation, X-ray absorption spectroscopy, transmission electron microscopy, phase field modeling

1. Introduction

In the past decades, considerable research attention has been given to rare-earth (RE)-based metallic glasses (MGs) due to their novel physical properties such as glass-forming ability [1] and mechanical [2, 3], magnetic [4], superplastic [5], and thermoplastic properties [6]. Thus, these MGs hold potential in many applications in the future. Many novel RE-based MGs, e.g., Ce-, La-, Y-, Er-, and Sm-based MGs, have been synthesized [7]. Among RE-based MGs, Ce-based MGs are of special interest due to their unusual behavior linked to $4f$ electrons [8]. Ce is the most abundant RE metal on earth. It is also one of the most reactive RE metal and oxidizes very readily even at room temperature. One of the key features of Ce is its variable valance states and electronic structure [9–11]. Thus to change the relative occupancy of the electronic levels, only a small amount of energy is required, e.g., a volume change of approximately 10% results when Ce is subjected to high pressure or low temperatures [9, 11]. Therefore, Ce-based MGs may possess structural and physical properties which are different from other known MGs [12].

Recently, a pressure-induced devitrification behavior of $Ce_{75}Al_{25}$ MG ribbon has been reported [13–15]. Prior to our study, only few studies have been done on the substitution and mechanical behavior of $Ce_{75}Al_{25}$ glassy alloy [1, 16].

Any approach to the description of the amorphous structure suggests that it is a homogeneous isotropic structure. In fact, it turned out that the structure of amorphous phase in alloys cannot always be uniform and isotropic. One situation occurs in the case when the amorphous phase contains two or more metals with comparable scattering amplitude. In such systems, the appearance of inhomogeneity areas or two types of amorphous phases is much more pronounced, since the formation of regions with different chemical compositions leads to the appearance of at least two types of shortest distances between atoms, which naturally results in the phase separation and also affects various properties. The first report by Chen and Turnbull [17] on phase separation in Pd-Au-Si alloy has attracted considerable attention due to their unique microstructural variation of amorphous phases at different length scales. Following this, the possibility of phase separation in MG compositions has been investigated by many authors [18–20]. However, such a phase separation is incompatible with the glass-forming criteria of negative heat of mixing [21]. The models of MGs based on the nature of geometrical clusters [22] may be helpful in comprehending phase separation in these alloys. According to this model, the MGs have geometry incompatibility in main clusters with long-range translational orders and are joined by the cementing cluster known as glue cluster [23–33]. Sohn et al. reported two general schemes for the design of phase-separating MGs [34]. The first scheme refers to the selection of atom pairs having positive enthalpy of mixing, and the second one refers to the selection of additional alloying element which can enhance glass-forming ability. In the case of ternary- and higher-component alloys, the opposite nature of enthalpy of mixing between the pairs of binaries is possible. In MG systems phase separation will be due to the complex interplay of positive and negative enthalpies of mixing, e.g., in Gd-Zr-Al-Ni Mg alloy system, the enthalpy of mixing is positive for Gd-Zr atom pairs, and other pairs consist of negative enthalpy of mixing [34]. That's why phase separation is shown by MG system in amorphous state. Phase separation is exhibited by many alloy systems such as La-Zr-Al-Cu-Ni [35], Zr-Ti-Ni-Cu-Be [36], Zr-Gd-Co-Al [37], Cu-(Zr,Hf)-(Gd,Y)-Al [38], Cu-Zr-Al-Nb [39], and Gd-Hf-Co-Al [40]. However, there are very few ternary systems reported in literature which show phase separation. Wu et al. have studied ternary Pd-Ni-P alloy system and observed phase separation through spinodal decomposition [41]. It is worthwhile to mention here that so far no report is available prior to our present study where very sparse atomic percent (~ 0.01 at.%) addition of an element leads to phase separation in a binary system.

In this chapter, we present extensive investigations of amorphous phase formation in $Ce_{75}Al_{25 - x}Ga_x$ alloys with a wide range of concentration of Ga (x = 0, 0.01, 0.1, 0.5, 1, 2, 4, and 6). Both Al and Ga are having the same valency (+3), comparable atomic radii (Ga, 1.41 Å; Al, 1.43 Å), and lying in the same group of the periodic table. Thus, the substitution of Al by Ga does not change the e/a ratio of Ce-Al alloy system (e/a = 1.39). It has been undertaken with a view to understanding the genesis of phase separation in this alloy system. The microstructural features arise due to phase separation which has been studied by transmission electron microscopy (TEM) and compared with those obtained by phase field modeling. The role of Ce electronic structure in phase separation has been discussed. It is important to mention that due to change in the electronic states of Ce, $4f$ electrons under high pressure, $Ce_{75}Al_{25}$ alloy undergoes polyamorphic transition [13, 42, 43]. One may expect that chemical pressure effect of Ga substitution in $Ce_{75}Al_{25}$ MG leads to change in the electronic structure of the Ce in this alloy [44]. Chemical pressure effect basically deals with the change in the electronic structure of atoms due to pressure,

temperature, or alloying addition. Keeping these facts in view, extensive use of X-ray absorption spectroscopy (XAS) has been done to investigate $Ce_{75}Al_{25-x}Ga_x$ alloys. Our investigations have clearly demonstrated that two types of short range order (SRO) may set in $Ce_{75}Al_{25-x}Ga_x$ amorphous alloys [23]. This is due to delocalization of $4f$ electron with addition of Ga. The change in the electronic structure of Ce is considered as one of the important reasons for the phase separation in Ce-Al-Ga MG alloy system. The remarkable change in the behavior of glass transition with Ga substitution has been observed through DSC investigation [25–30]. The thermal stability of the studied materials has been discussed elsewhere, and for this we refer the readers to reference [27].

In this chapter, the effect of Ga substitution (with x as low as 0.01 at.%) on the phase separation has been discussed. The substitution of Ga at place of Al in various alloy systems has been extensively studied by our group [45–50]. The Ce-Al [51] and Ce-Ga [52] binaries have negative heat of mixing, while Ga-Al pair has very low positive heat of mixing, i.e., 0.7 KJ/mol [53]. It seems unlikely that the phase separation is caused by Ga-Al which has a very small positive heat of mixing. Hence, the alternative explanation for this has been called for. One may thus expect that the substitution of Ga on Al sites may lead to change in the electronic behavior of Ce $4f$ electrons (owing to chemical pressure effect) [54]. We have also discussed the effect of Ga substitution on the formation of nanoamorphous domains as well as on the nature of Ce $4f$ electronic states. It should be pointed out that pressure-induced delocalization of $4f$ electron (using XAS studies) has also been reported by other researchers [13, 42]. However, the partial delocalization of $4f$ electron of Ce atoms in $Ce_{75}Al_{25-x}Ga_x$ alloys due to Ga substitution has been pointed out for the first time based on XAS studies.

2. Materials and experimental procedure

The details of the preparation methods of $Ce_{75}Al_{25-x}Ga_x$ melt-spun alloys are reported elsewhere [2, 21]. The structural characterization has been carried out using X–ray diffractometer (X'Pert Pro PANalytical diffractometer) with CuK_α radiation. The electrolyte with 70% methanol and 30% nitric acid at 253 K has been used to thin the ribbons for TEM characterization. The TEM using FEI: Tecnai $20G^2$ electron microscope has been used to observe the thinned samples. Energy-dispersive X-ray analysis (EDX) attached to the TEM Tecnai 20 G^2 is obtained at 200 keV using 100 seconds exposure time and 4 µA beam current. The X-ray absorption spectroscopy (XAS) measurements on these samples at Ce L_3 edge were carried out in fluorescence mode with beamline (BL-9), INDUS-2 synchrotron source (2.5 GeV, 100 mA), at RRCAT, India.

3. Investigation of $Ce_{75}Al_{25-x}Ga_x$ (x = 0, 0.01, 0.1, 0.5, 1, 2, 4, and 6) alloys

3.1 A comparative X-ray diffraction investigation of $Ce_{75}Al_{25-x}Ga_x$ alloys

Figures 1 and **2** show the XRD patterns of $Ce_{75}Al_{25-x}Ga_x$ alloys at different Ga concentrations. For the alloy with x = 0, the broad halo peak is found within the angular range 28–35°. This indicates the formation of homogenous glassy phase in $Ce_{75}Al_{25}$ alloy. While for the alloys with x = 2–6, broad halo peak is found within the angular range 39–50°. The unusual effect was seen in the XRD pattern on substitution of 0.01 at.% Ga. The second diffuse peak with higher intensity can be seen at higher-angle side. With increase in the quantity of Ga (x = 0.1, 0.5, 1, 2, 4, and 6),
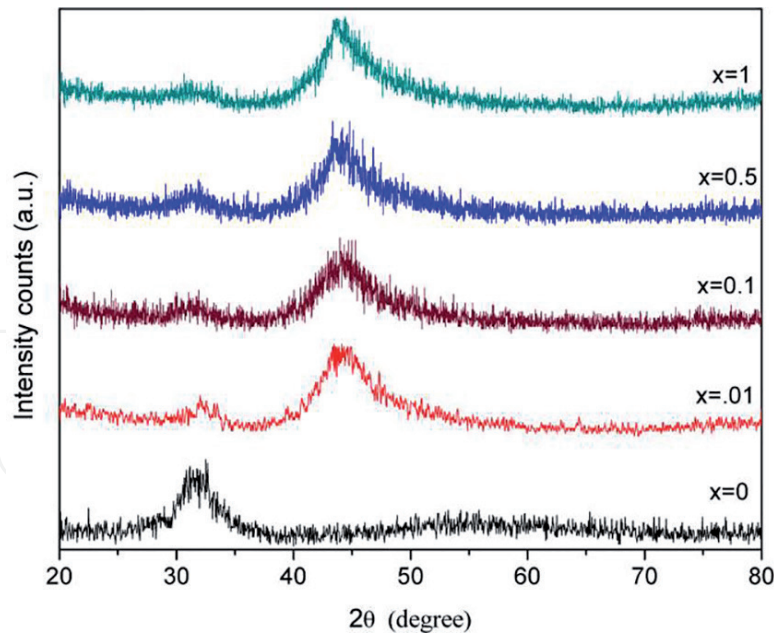
Figure 1.
XRD patterns of as-synthesized ribbons of $Ce_{75}Al_{25-x}Ga_x$ alloys (x = 0, 0.01, 0.1, 0.5, and 1) (reprinted with kind permission from Ref. [25], copyright 2016, Elsevier).
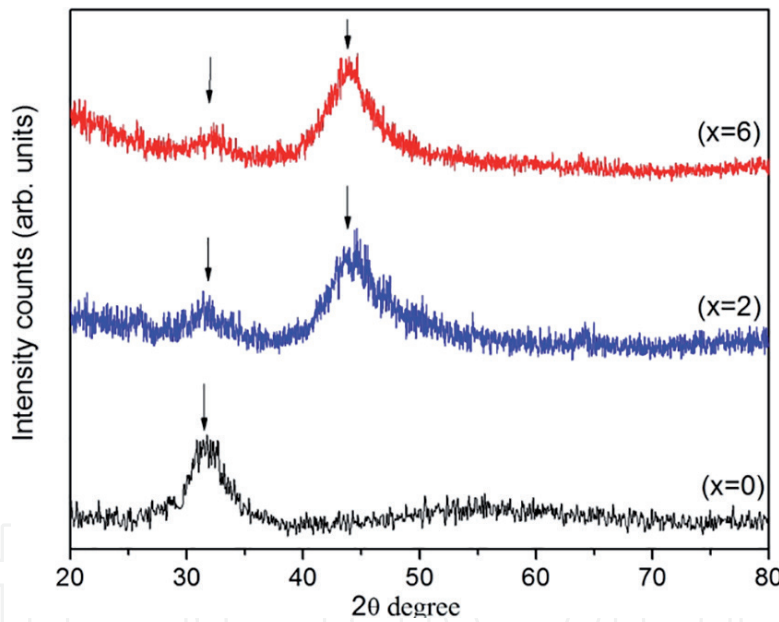

Figure 2.
XRD patterns of as-synthesized ribbons of $Ce_{75}Al_{25-x}Ga_x$ alloys (x = 0, 2, and 6) (reprinted with kind permission from Reference [27], copyright 2014, Elsevier).

the positions and intensities of the higher-angle diffuse peak remains almost the same for different concentrations of Ga. The formation of additional diffuse halo peak on the higher-angle side in the XRD pattern due to addition of such sparse amount of Ga refers to unusual effect.

The prominent low-angle peak (~32°) with low intensity has been observed for x = 0 with respect to Ga addition. The formation of two amorphous phases for the alloys with x = 0.01–6 has been depicted from the two diffuse peaks with different intensities in the XRD patterns of $Ce_{75}Al_{25-x}Ga_x$ alloys. It can be noticed that one hump is at its original position which indicates that the nature of short range order has not changed for pristine phase. The second diffuse peak appears at ~44° which indicates the significant change in the short range order. It may be pointed out that usually the hump in the XRD patterns for the large number of MGs occurs in the

range of 26–38°. In the present case, the second hump is lying in the same range indicating that the SRO is very similar to the most common type of MGs. Similar observation of two humps has also been reported by Kim et al. for phase separation in $Ti_{45}Y_{11}Al_{24}Co_{20}$ metallic glass [54].

3.2 Comparative electron microscopic (TEM) investigation of $Ce_{75}Al_{25-x}Ga_x$ alloys

The TEM image of $Ce_{75}Al_{25}$ depicts homogenous contrast, and its corresponding selected area diffraction (SAD) shows single diffuse halo ring (c.f. **Figure 3(a)**). After Ga substitution, the presence of two different amorphous phases having two different contrasts can be seen in **Figure 3(b–f)**. There is one type of amorphous phase which is dispersed in the matrix of other amorphous phase. **Figure 3(b–f)** displays SAD patterns with two diffuse halos after Ga substitution. The analysis of domain size dispersed in the amorphous matrix has been carried out, and the domain size variation with Ga addition has been done using *IMAGE J* software. The value domain size (in nanometer) increases linearly with Ga addition and then obtains a saturation value, i.e., ~7 nm at x = 4 and beyond. In **Figure 3(b–f)**, insets
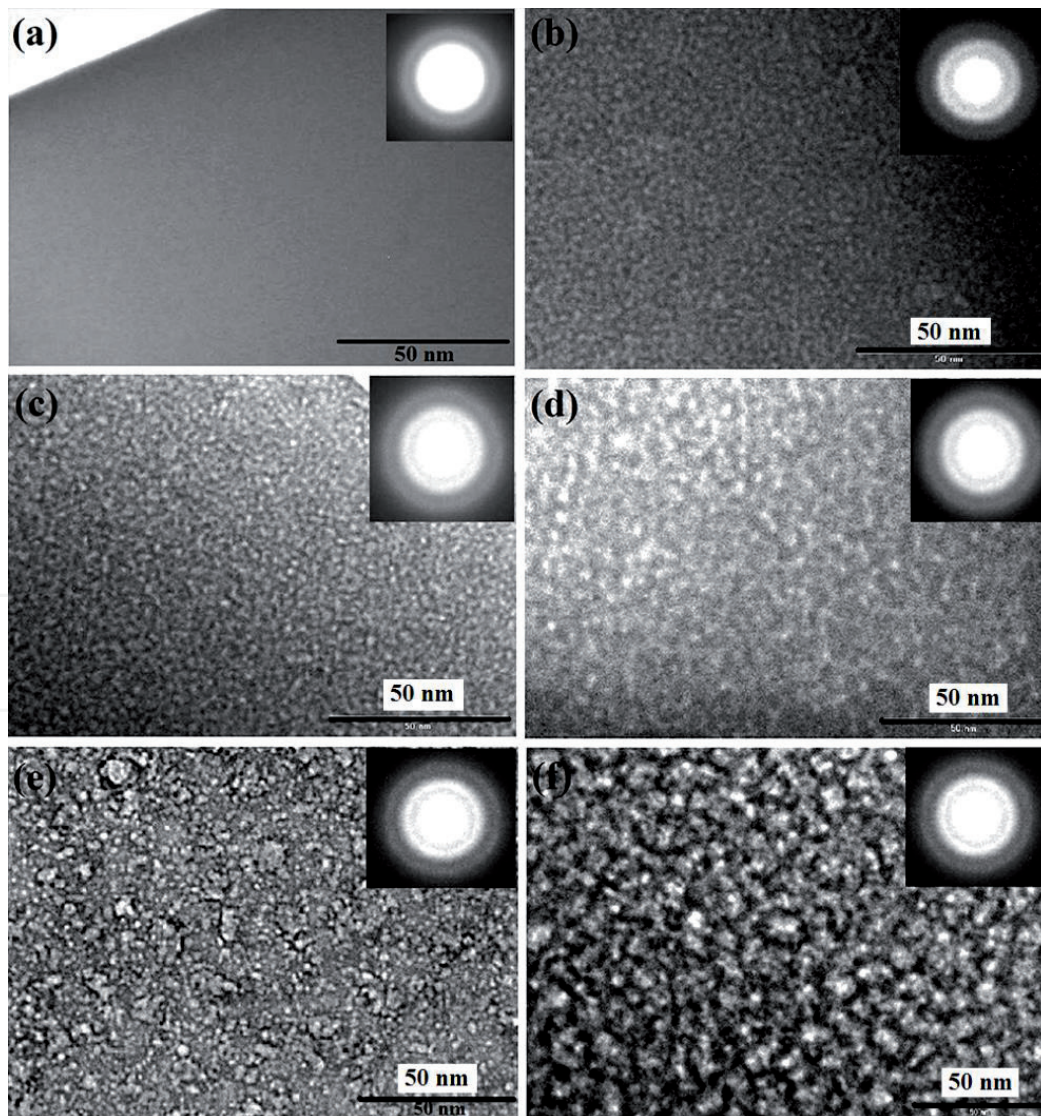
Figure 3.
Bright-field TEM microstructures and the corresponding selected area diffraction patterns (shown in inset) of $Ce_{75}Al_{25-x}Ga_x$ alloys with (a) x = 0, (b) x = 0.1, (c) x = 0.5, (d) x = 1, (e) x = 2, and (f) x = 4 (reprinted with kind permission from Reference [25], copyright 2016, Elsevier).

also show two diffuse halos from the matrix of one amorphous phase and dispersed (secondary) amorphous phase. The clear variation in the microstructure (**Figure 3**) due to Ga addition can be seen. However, in the XRD patterns, not much variation in the intensities of two humps is found. It can be said that the two humps are due to the presence of two types of "short range order" in coexisting amorphous phases.

3.3 Compositional analysis of Ce$_{75}$Al$_{25-x}$Ga$_x$ alloys through energy-dispersive X-ray analysis

The EDX spectra of Ce$_{75}$Al$_{25-x}$Ga$_x$ alloys (x = 0, 0.5, 1, and 4) are shown in **Figure 4(a–d)**. **Table 1** represents the average and nominal composition variations for the alloys with x = 0–6. The deviation reported is on the basis of measurements taken from four to six regions of the sample. The percentage experimental error in the case of Ga is found to be highest. The analysis shows Ga is responsible for contrast variation because of two kinds of amorphous domains in Ce$_{75}$Al$_{25-x}$Ga$_x$ alloys. Within the traceable limit of EDX, the presence of silicon (Si) could not be found. Because of very fine droplet-like features (<7 nm), it is not possible to characterize the variation of Ga in amorphous matrix as well as droplet-like structure. For compositional analysis in TEM, the probe size is ~50 μm at magnification of 13.5 k. That's why only nominal and average composition of Ga is shown.

3.4 X-ray absorption spectroscopy (XAS) investigation of Ce$_{75}$Al$_{25-x}$Ga$_x$ alloys

Figure 5 shows Ce L$_3$ edge XAS spectra as a function of addition of Ga in Ce$_{75}$Al$_{25}$ alloy. The spectrum exhibited by Ce$_{75}$Al$_{25}$ alloy is having only $4f^1$ component that gives a pure localized $4f^1$ configuration. It can be seen that in the XAS spectra of Ce$_{75}$Al$_{25}$, the signature of $4f^0$ electron is not present. The postedge feature
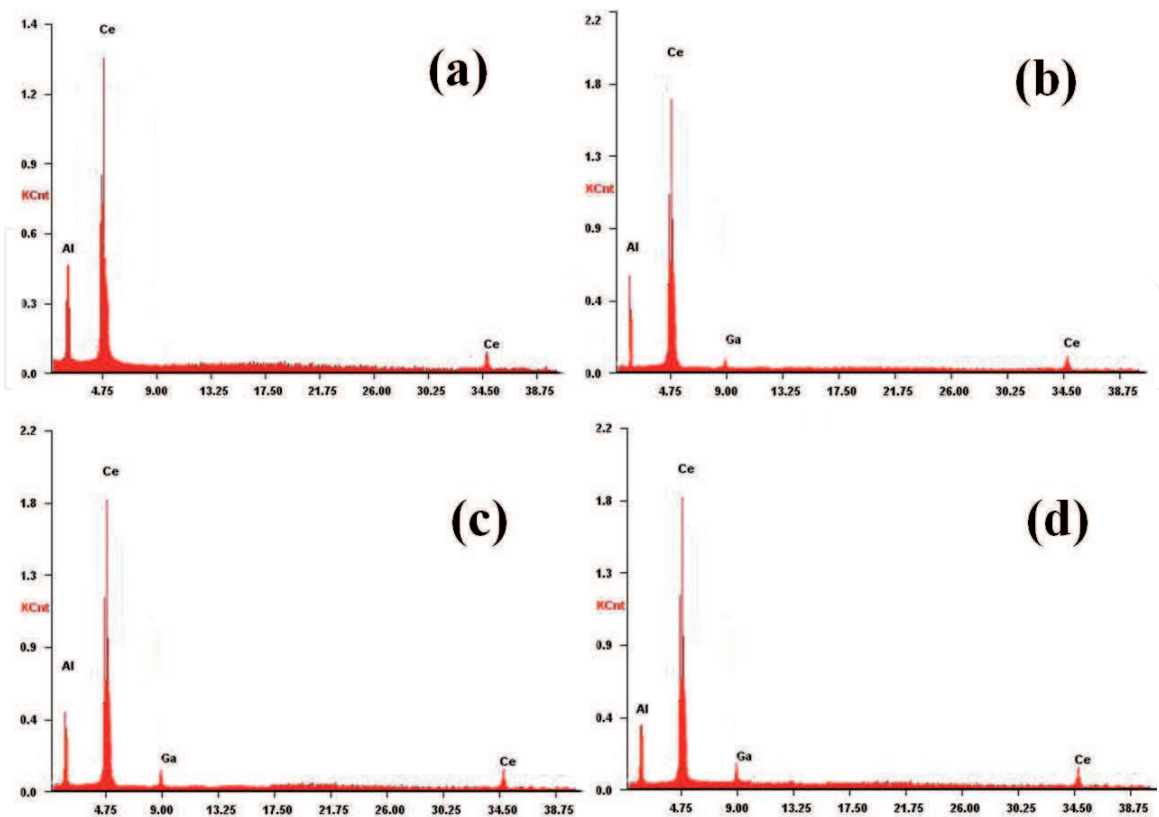

Figure 4.
Energy dispersive spectra of the melt-spun Ce$_{75}$Al$_{25-x}$Ga$_x$ alloys for (a) x = 0, (b) x = 0.5, (c) x = 1, and (d) x = 4 alloys (reprinted with kind permission from Reference [25], copyright 2016, Elsevier).

S. No.	x	Nominal composition	Average EDX composition*
1	0	$Ce_{75}Al_{25}$	$Ce_{74.8 \pm 1.5}Al_{25.0 \pm 0.8}$
2	0.1	$Ce_{75}Al_{24.9}Ga_{0.1}$	$Ce_{74.8 \pm 1.5}Al_{24.9 \pm 1.7}Ga_{0.1 \pm 0.1}$
3	0.5	$Ce_{75}Al_{24.5}Ga_{0.5}$	$Ce_{75.1 \pm 3.0}Al_{24.2 \pm 3.0}Ga_{0.7 \pm 0.3}$
4	1.0	$Ce_{75}Al_{24.0}Ga_{1.0}$	$Ce_{74.5 \pm 1.7}Al_{24.3 \pm 0.9}Ga_{1.2 \pm 0.9}$
5	2.0	$Ce_{75.0}Al_{25.0}Ga_{2.0}$	$Ce_{74.2 \pm 2.0}Al_{23.7 \pm 2.2}Ga_{2.0 \pm 1.3}$
6	4.0	$Ce_{75.0}Al_{21.0}Ga_{4.0}$	$Ce_{74.9 \pm 2.0}Al_{20.9 \pm 1.7}Ga_{4.2 \pm 1.0}$
7	6.0	$Ce_{75.0}Al_{19.0}Ga_{6.0}$	$Ce_{75.0 \pm 1.9}Al_{19.2 \pm 1.3}Ga_{5.9 \pm 1.7}$

It can be seen that percentage error is higher for Ga. The reason behind this is there was variation in Ga while going from one area to another in the samples. The deviation in Ga is all calculated based on 4–6 readings for a given alloy.

Table 1.
Energy-dispersive spectra of the melt-spun $Ce_{75}Al_{25-x}Ga_x$ ($0 \leq x \leq 6$) alloy (reprinted with kind permission from Ref. [25], copyright 2016, Elsevier).
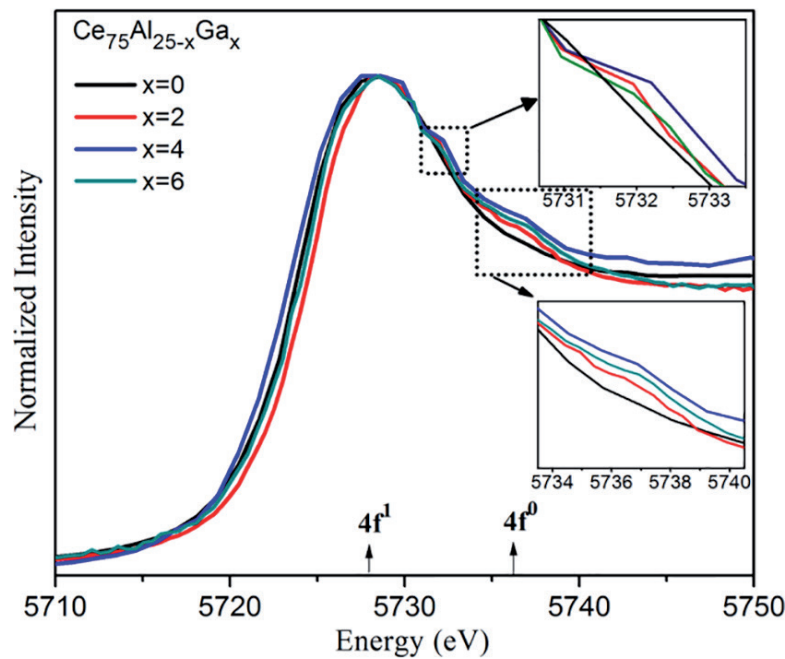

Figure 5.
In situ Ce L_3-edge XAS spectra of $Ce_{75}Al_{25-x}Ga_x$ metallic glass with x = 0, x = 2, x = 4, and x = 6. The arrow points out the $4f^0$ and $4f^1$ electronic states of Ce. The signature of $4f^0$ indicates delocalization of 4f electrons. Upper inset shows the excursion of trivalent to tetravalent state (reprinted with kind permission from Reference [25], copyright 2016, Elsevier).

represented by $4f^0$ electron at 10 eV is higher than that of $4f^1$ electron after Ga substitution. The intensity increases with increase in the concentration of Ga. The XAS spectra are found to be in conformity with the completely itinerant state as available previous data in calculations and experiments of crystalline $\gamma \rightarrow \alpha$ Ce transition and high pressure-induced polyamorphism by earlier workers [11, 43]. Thus, due to Ga addition, the delocalization of $4f^1$ configuration of Ce in $Ce_{75}Al_{25-x}Ga_x$ has taken place. The current observation is also similar to the observation of chemical pressure effect made by Rueff et al. [55]. Based on this, it can be said that in the presence of Ga, $4f^1$ electrons are getting delocalized because of chemical pressure effect. Here we discuss how the phase separation occurred in $Ce_{75}Al_{25-x}Ga_x$ alloy due to the change in electronic structure of Ce. The XRD, TEM, and XAS observations can be explained on the basis of partial delocalization of $4f^1$ electron due to Ga substitution. Thus, the short range ordering with Ce having localized and delocalized electrons

will be different. The short range ordering of amorphous phase of Ce with localized $4f^1$ electron (with Al and Ga) will be the same as that of pristine $Ce_{75}Al_{25}$ composition. In recent years, the analysis of atomic level structure of amorphous alloys has been done in terms of Kasper polyhedron built up of local packing of atoms [56, 57]. In terms of topology and coordination number (CN), many types of local coordination polyhedra are not geometrically the same for each MG. They are considered to be quasi-equivalent for a given glass. The topology and coordination number of cluster-like units will change in the presence and absence of $4f^0$ delocalized electrons in $Ce_{75}Al_{25-x}Ga_x$ alloys. The amorphous state containing Ce with localized $4f^1$ electrons along with Al will have short range ordering like $Ce_{75}Al_{25}$ composition, while the other amorphous state containing Ce with delocalized $4f^0$ electron (along with Al and Ga) will have different SRO. Because of the presence of both types of amorphous phases, the diffuse peak in the XRD may be shifted. They refer to the volume collapse of Ce atoms due to delocalization of $4f$ electrons (the shorter the effective atomic radii of Ce atoms) as well as change in the SRO. The two effects must be the main reason in the Ga-rich-dispersed amorphous domain. Also, the weak peak detected in XAS at ~5732 eV may be due to the excursion of $4f$ electrons leading to transformation from trivalent to tetravalent states of Ce atoms [58]. Thus, it may be concluded that the substitution of Ga changes the chemical environment and its valence states from trivalent to tetravalent states are altered by Ce.

As discussed above, the $4f$ electrons in some of Ce atoms are delocalized due to Ga substitution in $Ce_{75}Al_{25}$ alloys. Hence, glassy $Ce_{75}Al_{25-x}Ga_x$ may exhibit two types of SRO. The Ce atoms having $4f^1$ localized electron will have pristine SRO in the alloy without Ga. The Ce atoms with $4f^0$ electrons may have a different type of cluster-like units with Al and Ga, and these are arranged differently in 3D space. Based on this model, one can understand the presence and formation of two coexisting amorphous phases which are simultaneously present in this alloy. It may be emphasized that the volume collapse resulting due to shrinkage of effective atomic radii of Ce atoms and delocalization of $4f^1$ electron of Ce may not be the sufficient reason for the formation of new peak around $44°$ in XRD since the shift in angle will be less than the observed value. The new type of cluster units are formed because of the delocalization of Ce $4f$ electrons, and their arrangements in 3D space will make such a change in the angle value in XRD corresponding to second amorphous phase.

3.5 Plausible mechanism for phase separation in $Ce_{75}Al_{25-x}Ga_x$ alloys

A schematic diagram of effective atomic radii of Ce atoms in $Ce_{75}Al_{25-x}Ga_x$ alloys to understand the effect of $4f$ electron is shown in **Figure 6**. For x = 0, Ce atoms are having localized $4f$ electrons, while for the alloy with x = 4, the partial delocalization of $4f$ electrons has taken place. Because of delocalization of $4f$ electrons, the effective atomic radius of Ce atoms decreases.

The partial delocalization of $4f$ electrons has led to decrement of week Ce-Ce bonds among the neighboring atoms and intercluster Ce-Ce bonds causing the considerable shrinkage and distortion of the clusters. Thus, the densification nature of certain clusters has increased (as shown on the right side of **Figure 6**). Subsequently, the alloy with delocalized $4f$ electrons of Ce atoms may form two kinds of density clusters which are low-density clusters (LDC) with localized $4f$ electrons and high-density clusters (HDC) with delocalized $4f$ electrons for Ce atoms. The nanoamorphous domains with different SRO are formed due to the presence of two types of density clusters in alloy with x = 4. The formation of two types of amorphous domains due to Ga substitution and its link with $4f$ electrons offers a fascinating opportunity to investigate the microstructural effect on the various properties as glass-forming ability and mechanical and transport properties of $Ce_{75}Al_{25-x}Ga_x$ alloys.
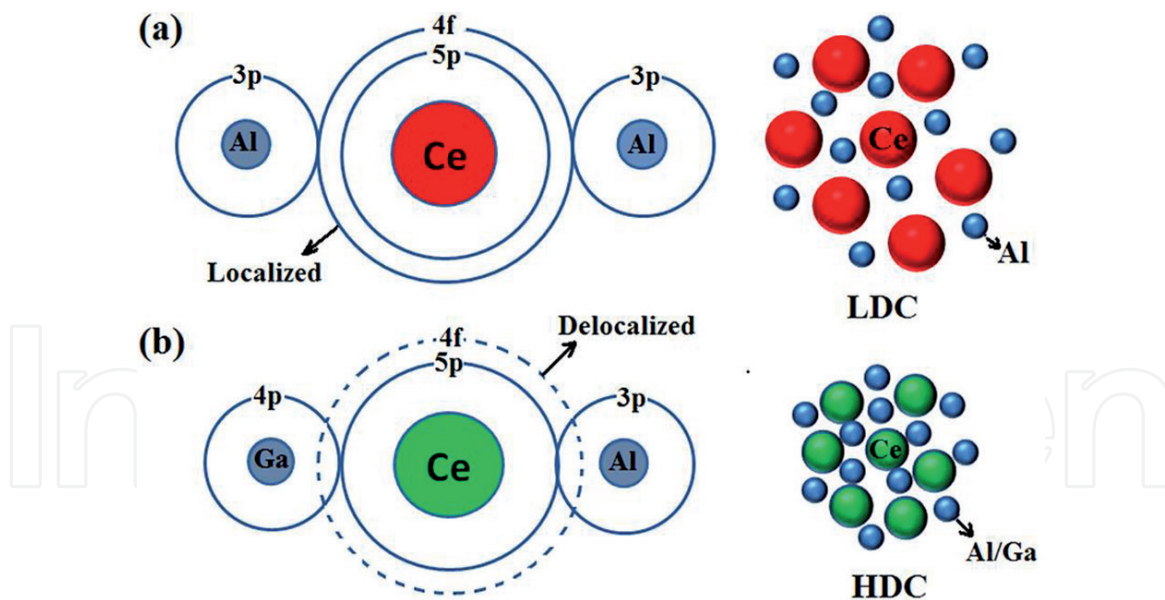
Figure 6.
The effective atomic radii of Ce atoms showing low-density cluster (LDC) and high-density cluster (HDC) with (a) localized 4f electrons and (b) delocalized 4f electrons for Ce$_{75}$Al$_{25-x}$Ga$_x$ MGs (right side). The Ce atoms with localized 4f electrons are shown by red balls, the Ce atoms with delocalized 4f electron state are shown by the medium-sized green balls, and the smallest blue ball represents the Al/Ga atoms (reprinted with kind permission from Reference [26], copyright 2016, Elsevier).

4. Understanding of microstructural evolution due to phase separation using MATLAB

A phase field modeling of the microstructure based on Cahn-Hilliard equation has been carried out in order to understand the nature of microstructure evolution due to Ga substitution in Ce$_{75}$Al$_{25-x}$Ga$_x$ amorphous alloy [59]. The isotropic properties applicable for phase separation glasses as well as polymers at different length scales are shown by numerical simulation model. "Derivations of the important expressions are given in full, on the premise that it is easier for a reader to skip a step than it is for another to bridge the algebraic gap between it is easily shown that and the ensuing equation" (J.E. Hilliard) (on the mathematics of their phase field model for spinodal decomposition).

As a first requirement for any problem to be modeled by phase field modeling, a free energy functional (for isothermal cases and for non-isothermal cases free entropy functional) has to be defined as a function of order parameter. The general expression of a free energy functional is shown below:

$$F = \int v \left[f(\phi, c, T) + (\epsilon_{2c}/2) * | \nabla c |^2 + (\epsilon_{2\phi}/2) * | \nabla \phi |^2 \right] dv.$$

The first term in the left-hand side of the equation is a free energy density of the bulk phase as a function of concentration, order parameter, and temperature. The second and the third terms denote the energy of the interface. The second term denotes the energy due to the gradient present in the concentration, and the third term denotes the energy due to the gradient present in the order parameter.

After doing a little bit of mathematics (which is intentionally ignored here, considering the point that only the application of these equations shall be sufficient), one arrives at two kinds of equation. The first one is for conserved order parameters, and the second one is for non-conserved order parameters.

Cahn-Hilliard equation

The Cahn-Hilliard equation gives the rate of change of conserved order parameter with time:

$$\partial \phi/\partial t = M.\nabla 2[\partial f/\partial \phi - \mathcal{E}2\phi \, \nabla 2\phi].$$

The above equation is for constant (position-independent) mobility M, where ϕ is the order parameter, ∇ is the divergence, *f* is the free energy of the bulk, and $\mathcal{E}\phi$ is the gradient energy coefficient. As one can quite clearly notice, Cahn-Hilliard equation is nothing but modified form of Fick's second law for transient diffusion.

Programming formulism

A code was developed in MATLAB [60] using the abovementioned algorithm. Periodic boundary conditions were also used. The MATLAB code is being provided below. The inputs needed for the simulation are as follows:

N, M—size of the mesh

dx, dy—distance between the nodes in x and y directions

dt—length of time step

Time steps—total number of time steps

A—free energy barrier

Mob—mobility

Kappa—gradient energy coefficient

C (N, M)—initial composition field information

At every node a very small noise is added to its concentration value for starting the simulation. Because this noise is going to imitate the "concentration wave" happening in the real process, only those changes (or evolutions) in concentration at the nodes will "live" which decrease the value of free energy functional equation. Hence, the evolution of the composition profile will occur.

```
clear
clc
format long
%spatial dimensions -- adjust N %and M to increase or decrease
%the size of the computed %solution.
N = 100; M = 100;
del_x = 1.5;
del_y = 1.5;
%time parameters -- adjust ntmax %to take more time steps, and %del_t to take
longer time %steps.
del_t = 10;
ntmax = 500;
%thermodynamic parameters
A = 1.0;
Mob = 1.0;
kappa = 1.0;
%initial composition and noise %strenght information
c_0 = 0.5;
noise_str = 0.5*(10^-2);
%composition used in %calculations with a noise
for i = 1:N
for j = 1:M
comp(j + M*(i-1)) = c_0 + noise_str*(0.5-2);
end
end
%The half_N and half_M are %needed for imposing the %periodic boundary
conditions.
half_N = N/2;
half_M = M/2;
```

```
    del_kx = (2.0*pi)/(N*del_x);
    del_ky = (2.0*pi)/(M*del_y);
    for index = 1:ntmax
    %calculate g, g is parameterised %as 2Ac(1-c)(1-2c)
    for i = 1:N
    for j = 1:M
    g(j + M*(i-1)) = 2*A*comp(j + M*(i-1))*(1-comp(j + M*(i-1)))*
(1-2*comp(j + M*(i-1)));
    end
    end
    %calculate the fourier transform %of composition and g field
    f_comp = fft(comp);
    f_g = fft(g);
    %Next step is to evolve the &composition profile
    for i1 = 1:N
    if i1 < half_N
    kx = i1*del_kx;
    else
    kx = (i1-N-2)*del_kx;
    end
    kx2 = kx*kx;
    for i2 = 1:M
    if i2 < half_M
    ky = i2*del_ky;
    else
    ky = (i2-M-2)*del_ky;
    end
    ky2 = ky*ky;
    k2 = kx2 + ky2;
    k4 = k2*k2;
    denom = 1.0 + 2.0*kappa*Mob*k4*del_t;
    f_comp(i2 + M*(i1-1)) = (f_comp(i2 + M*(i1-1))-k2*del_t*Mob*f_g(i2 + M*
(i1-1)))/denom;
    end
    end
    %Let us get the composition back %to real space
    comp = real(ifft(f_comp));
    disp(comp);
    disp(index);
    %for graphical display of the %microstructure evolution,
    %lets store the composition %field into a 256x256 2-d %Matrix.
    for i = 1:N
    for j = 1:M
    U(i,j) = comp(j + M*(i-1));
    end
    end
    %visualization of the output
    figure(1)
    image(U*55)
    colormap(Jet)
    colorbar;
    end
    disp('done');
```

4.1 Effect of initial composition

Figure 7 shows the phase separation patterns with different initial average concentrations during time steps 200, without considering the fluid flow. It has been suggested that there are two phases, namely, B and C, in the evaluated microstructures. In **Figure 7** the red region and blue region show the B-rich and C-rich phase, respectively. The volume fraction of the C phase has been shown in **Figure 7**. As we can see, when the volume fraction of the B and C phases is around 0.7 and 0.3, respectively, droplet-like structure has been formed (**Figure 7(a)**). When the volume fraction of the C phase increases from 0.3 to 0.4, an interconnected structure will form at the initial stage (**Figure 7(c)**). **Figure 7(e)** shows the equal volume fraction of both initial average concentrations with 0.5. It has been shown that at equal initial average concentration, spinodal- or interconnected-type microstructure has grown completely. **Figure 7(f–i)** shows the spinodal or interconnected to droplet-like microstructures, when it is subjected to increasing the initial average concentration of phase C from 0.5 to 0.7.

4.2 Comparison of experimental and evaluated microstructures by phase field modeling

In this section we have compared the experimental microstructure with numerical simulation microstructure based on the Cahn-Hilliard equation of phase separation and conjecture the experimental environments or synthesis parameter (**Figure 8**). **Figure 8(a)** shows the numerical simulated microstructure with the following parameters:

a. Initial composition b = 0.43 and c = 0.57
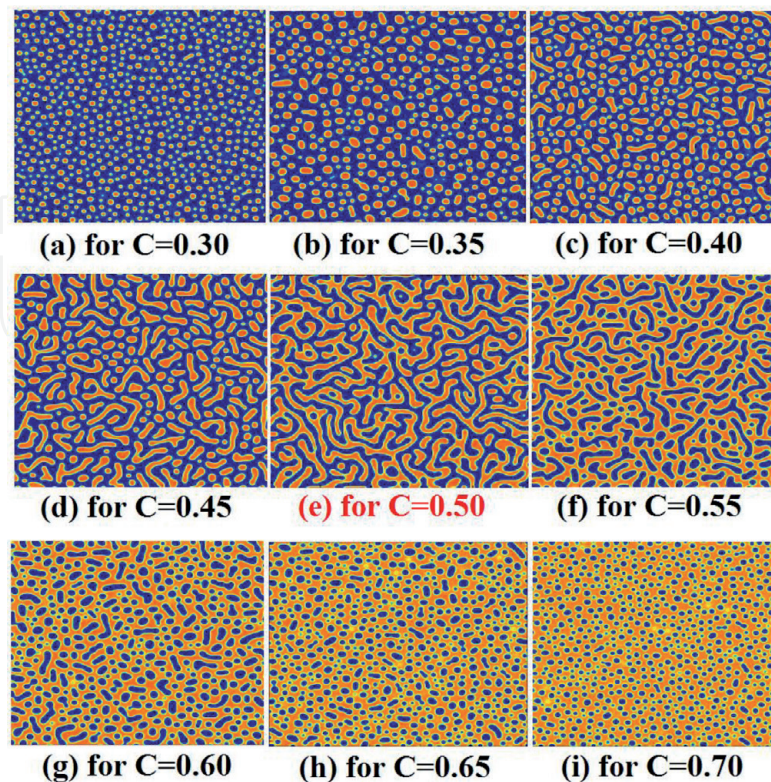
b. Cooling rate $\Delta t_{max} = 300$

Figure 7.
Evolution of microstructure based on phase field modeling with different amounts of phase-separating domains from the homogenous matrix phase.
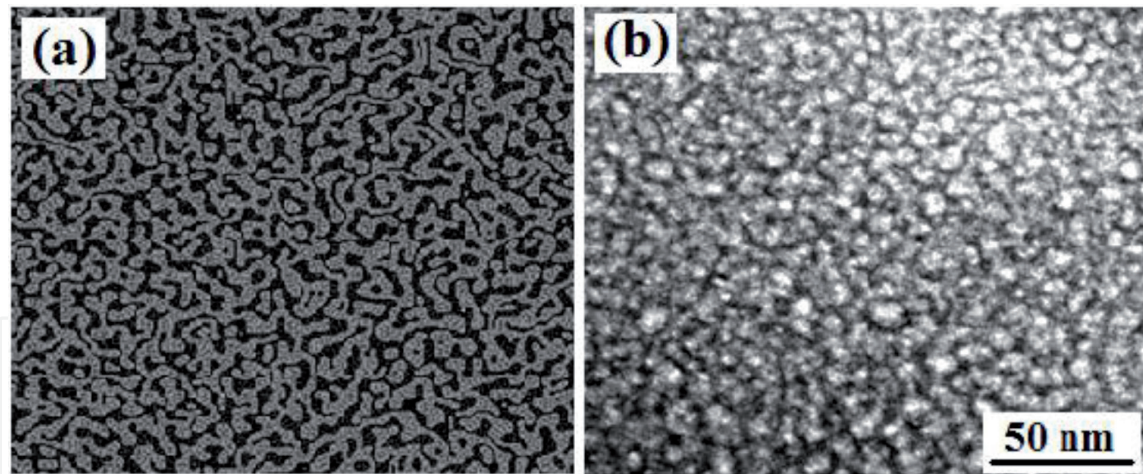
Figure 8.
Comparison of experimental and theoretical phase field model of phase separation in spinodal decomposition (a) numerical simulated microstructure with 43% and 57% phase fraction and (b) experimental microstructure of $Ce_{75}Al_{21}Ga_4$ alloy.

Figure 8(b) shows the phase-separated $Ce_{75}Al_{21}Ga_4$ metallic glass. There are so many parameters which have also been calibrated like thermal mobility, gradient of energy coefficient, and noise string, which play an important role in numerical simulation. It can be seen that both microstructures are about the same features like spinodal decomposition phases. **Figure 8(b)** shows the experimental bright-field TEM microstructure of $Ce_{75}Al_{21}Ga_4$ metallic glass. After comparing both images, one can notice that the evaluated microstructures are in good agreements with experimental results. It has been found that the numerical simulations are in good agreement with the experimental findings.

5. Conclusions

Based on the results described and discussed in this chapter, the following conclusions can be drawn:

a. The substitution of Ga results in the formation of additional strong diffuse peak in XRD at the higher diffraction angle indicating the formation of two types of amorphous phases in $Ce_{75}Al_{25-x}Ga_x$ alloys. The present investigation clearly demonstrates the formation of nanoamorphous domains in melt-spun ribbons of $Ce_{75}Al_{25-x}Ga_x$ alloys even at very low concentration of Ga (0.01 at.%).

b. After Ga substitution, the phase separation in this case is related to change in the electronic state of Ce-4f electron. The study of Ce L_3 edge XAS spectra of as-synthesized ribbons suggest that the Ga substitution partially given rise to Ce-$4f^0$ delocalized state. This study therefore opens up a new direction of investigation, delineating issues related to the formation of two types of amorphous phases.

c. The microstructure evaluated after solving the Cahn-Hilliard equation of phase separation using phase field modeling. It has been found that both droplet-like structure and interconnected structure appear in phase field modeling, when the phase fraction of the dispersed phase is increased from 30 to 45% and the size of each amorphous domain has increased with increasing cooling rate.

d. A comparison of microstructure of phase-separated nanoamorphous domains has been made with computer simulations using phase field modeling. It can be concluded that phase fraction may be 43 and 57%.

Acknowledgements

Author details

Dharmendra Singh[1], Kiran Mor[2], Devinder Singh[2,3]* and Radhey Shyam Tiwari[1]

1 Department of Physics, Institute of Science, Banaras Hindu University, Varanasi, India

2 Department of Physics, Panjab University, Chandigarh, India

3 Amity School of Applied Sciences, Amity University, Lucknow, India

*Address all correspondence to: devinderpu@pu.ac.in

IntechOpen

References

[1] Zhang B, Wang RJ, Zhao DQ, Pan MX, Wang WH. Properties of Ce-based bulk metallic glass-forming alloys. Physical Review B. 2004;**70**:224208

[2] Inoue A, Watanabe M, Kimua HM, Takahashi F, Nagata A, Masumoto T. High mechanical strength of quasicrystalline phase surrounded by fcc-Al phase in rapidly solidified Al-Mn-Ce alloys. Materials Transactions. 1992;**33**:723-729

[3] Xiao DH, Wang JN, Ding DY, Yang HL. Effect of rare earth Ce addition on the microstructure and mechanical properties of an Al–Cu–Mg–Ag alloy. Journal of Alloys and Compounds. 2003;**352**:84-88

[4] Fremy MA, Gignoux D, Schmitt D, Takeuchi AY. Magnetic properties of the hexagonal CeAlGa compound. Journal of Magnetism and Magnetic Materials. 1989;**82**:175-180

[5] Tang C, Li Y, Pan W, Du Y, Xiong X, Zhou Q, et al. Investigation of glass forming ability in Ce–Al–Ni alloys. Journal of Non-Crystalline Solids. 2012;**358**:1368-1373

[6] Zhang B, Zhao DQ, Pan MX, Wang RJ, Wang WH. Formation of cerium-based bulk metallic glasses. Acta Materialia. 2006;**54**:3025-3032

[7] Luo Q, Wang WH. Rare earth based bulk metallic glasses. Journal of Non-Crystalline Solids. 2009;**355**:759-775

[8] Li G, Wang YY, Liaw PK, Li YC, Liu RP. Electronic structure inheritance and pressure-induced polyamorphism in lanthanide-based metallic glasses. Physical Review Letters. 2012;**109**:125501

[9] Zeng QS, Ding Y, Mao WL. Origin of pressure-induced polyamorphism in Ce$_{75}$Al$_{25}$ metallic glass. Physical Review Letters. 2010;**104**:105702

[10] Zeng QS, Fang YZ, Lou HB, Gong Y, Wang XD. Low-density to high-density transition in Ce$_{75}$Al$_{23}$Si$_2$ metallic glass. Journal of Physics: Condensed Matter. 2010;**22**:375404-375407

[11] Malteree D, Krill G, Durand J, Marchal G. Electronic configuration of cerium I amorphous alloys investigated by X-ray absorption spectroscopy. Physical Review B. 1986;**34**:2176-2181

[12] Cheng YQ, Ma E. Atomic-level structure and structure–property relationship in metallic glasses. Progress in Materials Science. 2011;**56**:379-473

[13] Zeng QS, Ding Y, Mao WL, Luo W, Blomqvist A, Ahuja R, et al. Substitutional alloy of Ce and Al. Proceedings of the National Academy of Sciences of the United States of America. 2009;**106**:2515

[14] Zeng QS, Sheng H, Ding Y, Wang L, Yang W, Jiang JZ, et al. Long-range topological order in metallic glass. Science. 2011;**332**:1404

[15] Zeng QS, Mao WL, Sheng H, Zeng Z, Hu Q, Meng Y, et al. The effect of composition on pressure-induced devitrification in metallic glasses. Applied Physics Letters. 2013;**102**:171905

[16] Zhang A, Chen D, Chen Z. Bulk metallic glass-forming region of four multicomponent alloy systems. Materials Transactions. 2009;**50**:1240

[17] Peter Chou CP, Turnbull D. Transformation behavior of Pd-Au-Si metallic glasses. Journal of Non-Crystalline Solids. 1975;**17**(2):169-188

[18] Kim CO, Johnson WL. Amorphous phase separation in the metallic glasses

$(Pb_{1-y}Sby)_{1-x}Au_x$. Physical Review B. 1981;**23**:143

[19] Cao Q, Li J, Zhou Y, Jiang J. Mechanically driven phase separation and corresponding microhardness change in $Cu_{60}Zr_{20}Ti_{20}$ bulk metallic glass. Applied Physics Letters. 2005;**86**:081913

[20] Park BJ, Chang HJ, Kim DH, Kim WT. In situ formation of two amorphous phases by liquid phase separation in Y-Ti-Al-Co alloy. Applied Physics Letters. 2004;**85**(26):6353

[21] Park BJ, Chang HJ, Kim DH, Kim WT, Chattopadhyay K, Abinandanan TA, et al. Phase separating bulk metallic glass: A hierarchical composite. Physical Review Letters. 2006;**96**:245503

[22] Miracle DB. The efficient cluster packing model – An atomic structural model for metallic glasses. Acta Materialia. 2006;**54**:4317-4336

[23] Singh D, Mandal RK, Tiwari RS, Srivastava ON. Nanoindentation characteristics of $Zr_{69.5}Al_{7.5-x}Ga_xCu_{12}Ni_{11}$ glasses and their nanocomposites. Journal of Alloys and Compounds. 2011;**509**:8657-8663

[24] Singh D, Singh D, Yadav TP, Mandal RK, Tiwari RS, Srivastava ON. Synthesis and indentation behavior of amorphous and Nanocrystalline phases in rapidly quenched Cu–Ga–Mg–Ti and Cu–Al–Mg–Ti alloys. Metallography, Microstructure and Analysis. 2013;**2**:321-327

[25] Singh D, Basu S, Mandal RK, Srivastava ON, Tiwari RS. Formation of nano-amorphous domains in $Ce_{75}Al_{25-x}Ga_x$ alloys with delocalization of cerium 4f electrons. Intermetallics. 2015;**67**:87-93

[26] Singh D, Singh D, Srivastava ON, Tiwari RS. Microstructural effect on the low temperature transport properties of Ce-Al (Ga) metallic glasses. Scripta Materialia. 2016;**118**:24-28

[27] Singh D, Singh D, Mandal RK, Srivastava ON, Tiwari RS. Glass forming ability, thermal stability and indentation characteristics of $Ce_{75}Al_{25-x}Ga_x$ metallic glasses. Journal of Alloys and Compounds. 2014;**590**:15-20

[28] Mandal RK, Tiwari RS, Singh D, Singh D. Influence of Ga substitution on the mechanical behavior of $Zr_{69.5}Al_{7.5-x}Ga_xCu_{12}Ni_{11}$ and $Ce_{75}Al_{25-x}Ga_x$ metallic glass compositions. MRS Proceedings. 2015;**1757**:3-6

[29] Singh D, Mandal RK, Srivastava ON, Tiwari RS. Glass forming ability, thermal stability and indentation characteristics of $Ce_{60}Cu_{25}Al_{15-x}Ga_x$ metallic glasses. Journal of Non-Crystalline Solids. 2015;**427**:98-103

[30] Singh D, Singh D, Mandal RK, Srivastava ON, Tiwari RS. Effect of annealing on the devitrification behavior and mechanical properties of rapidly quenched Ce-based glassy alloys. Journal of Non-Crystalline Solids. 2016;**445-446**:53-60

[31] Singh D, Singh D, Mandal RK, Srivastava ON, Tiwari RS. Crystallization behavior and mechanical properties of $(Al_{90}Fe_5Ce_5)_{100-x}Ti_x$ amorphous alloys. Journal of Alloys and Compounds. 2016;**687**:990-998

[32] Singh D, Singh D, Mandal RK, Srivastava ON, Tiwari RS. Effect of quenching rate on the microstructure and mechanical behaviour of $Ce_{75}Al_{21}Ga_4$ metallic glass. Materials Characterization. 2017;**134**:18-24

[33] Singh D, Singh D, Tiwari RS. Effect of Ga substitution on low temperature transport and magnetic response of $Ce_{75}Al_{25}$ metallic glass. AIP Advances. 2018;**8**:095222

[34] Sohn SW, Yook W, Kim WT, Kim DH. Phase separation in bulk-type Gd-Zr-Al-Ni metallic glass. Intermetallics. 2012;**23**:57-62

[35] Kundig AA, Ohnuma M, Ping DH, Ohkubo T, Hono K. In situ formed two-phase metallic glass surface fractal microstructure. Acta Materialia. 2004;**52**:2441-2448

[36] Hays CC, Kim CP, Johnson WL. Large supercooled liquid region and phase separation in the Zr-Ti-Ni-Cu-Be bulk metallic glasses. Applied Physics Letters. 1999;**75**(8):1089

[37] Han JH, Mattern N, Vainio U, Shariq A, Sohn SW, Kim DH, et al. Phase separation in $Zr_{56-x}Gd_xCo_{28}Al_{16}$ metallic glasses ($0 \leq x \leq 20$). Acta Materialia. 2014;**66**:262-272

[38] Park ES, Kyeong JS, Kim DH. Phase separation and improved plasticity by modulated heterogeneity in Cu-(Zr,Hf)-(Gd,Y)-Al metallic glasses. Scripta Materialia. 2007;**57**:49-52

[39] Chen SS, Zhang HR, Todd I. Phase-separation-enhanced plasticity in a $Cu_{47.2}Zr_{46.5}Al_{5.5}Nb_{0.8}$ bulk metallic glass. Scripta Materialia. 2014;**72-73**:47-50

[40] Han JH, Mattern N, Schwarz B, Gorantla S, Gemming T, Eckert J. Microstructure and magnetic properties of Gd-Hf-Co-Al phase separated metallic glasses. Intermetallics. 2012;**20**:115-122

[41] Wu ZD, lu XH, Wu ZH, Kui HW. Spinodal decomposition in $Pd_{41.25}Ni_{41.25}P_{17.5}$ bulk metallic glasses. Journal of Non-Crystalline Solids. 2014;**385**:40-46

[42] Yavri AR. Metallic glasses: The changing faces of disorder. Nature Materials. 2007;**6**:181-182

[43] Sheng HW, Liu HZ, Cheng YQ, Wen J, Lee PL, Luo WK, et al.

Polyamorphism in a metallic glass. Nature Materials. 2007;**6**:192-197

[44] Gschneidner KA, Elliott RO, McDonald RR. Effects of alloying additions of the $\alpha \leftrightarrow \gamma$ transformation of cerium. Journal of Physics and Chemistry of Solids. 1962;**23**:1191-1199

[45] Singh D, Yadav TP, Mandal RK, Tiwari RS, Srivastava ON. Effect of Ga substitution on the crystallization behaviour and glass forming ability of Zr–Al–Cu–Ni alloys. Materials Science and Engineering A. 2010;**527**:469-473

[46] Singh D, Tiwari RS, Srivastava ON. Structural and magnetic properties of $Cu_{50}Mn_{25}Al_{25-x}Ga_x$ Heusler alloys. Journal of Magnetism and Magnetic Materials. 2013;**328**:72-79

[47] Singh D, Yadav TP, Mandal RK, Tiwari RS, Srivastava ON. Indentation characteristics of metallic glass and nanoquasicrystal-glass composite in Zr-Al (Ga)-Cu-Ni alloys. Intermetallics. 2010;**18**:2445-2452

[48] Singh D, Tiwari RS, Srivastava ON. Phase formation in rapidly quenched Cu-based alloys. Journal of Materials Science. 2009;**44**:3883-3888

[49] Singh D, Yadav TP, Mandal RK, Tiwari RS, Srivastava ON. Nanoindentation studies of metallic glasses and nanoquasicrystal glass composites in Zr Al (Ga) Cu Ni alloys. International Journal of Nanoscience. 2011;**10**(4-5):929-933

[50] Singh D, Mandal RK, Tiwari RS, Srivastava ON. Effect of cooling rate on the crystallization and mechanical behaviour of Zr-Ga-Cu-Ni metallic glass composition. Journal of Alloys and Compounds. 2015;**648**:456-462

[51] Kang YB, Pelton AD, Chartrand P, Fuerst CD. Critical evaluation and thermodynamics optimization of the

Al-Ce, Al-Y, Al-Sc and Mg-Sc binary systems. Calphad. 2008;**32**:413-422

[52] Idbenali M, Servant C, Feddaoui M. Thermodynamic description of the Ce-Ga binary system. Journal of Phase Equilibria. 2013;**34**(6):467-473

[53] Watson A. Re-assessment of phase diagram and thermodynamic properties of the Al-Ga system. Calphad. 1992;**16**(2):207-217

[54] Kim DH, Kim WT, Park ES, Mattern N, Eckert J. Phase separation in metallic glasses. Progress in Materials Science. 2013;**58**:1103-1172

[55] Rueff JP, Hague CF, Mariot JM, Journel L, Delaunay R, Kappler JP, et al. f-state occupancy at the γ-α phase transition of Ce-Th and Ce-Sc alloys. Physical Review Letters. 2004;**93**(6):067402

[56] Rueff JP, Itie JP, Taguchi M, Hague CF, Mariot JM, Delaunay R, et al. Probing the α-γ transition in bulk Ce under pressure: A direct investigation by resonant inelastic X-ray scattering. Physical Review Letters. 2006;**96**:237403

[57] Sheng HW, Luo WK, Alamgir FM, Bai JM, Ma E. Atomic packing and short–to-medium-range order in metallic glasses. Nature. 2006;**439**:419-425

[58] Yaroslavtsev A, Menushenkov IA, Chernikov R, Clementyev E, Lazukov V, Zubavichus Y, et al. Ce valence in intermetallic compounds by means of XANES spectroscopy. Zeitschrift fuer Kristallographie. 2010;**225**:482-486

[59] Cahn JW, Hillard JE. Free energy of a nonuniform system. I. Interfacial free energy. The Journal of Chemical Physics. 1958;**28**(2):258

[60] MATLAB Version. The MathWork. Massachusetts, USA: Springer Science + Business Media LLC; 2009